Journal of Hazardous Materials 161 (2009) 1122–1130

Contents lists available at ScienceDirect

Journal of Hazardous Materials

journal homepage: www.elsevier.com/locate/jhazmat

Synthesis and photocatalytic activity of stable nanocrystalline TiO_2 with high crystallinity and large surface area

Guohui Tian, Honggang Fu*, Liqiang Jing, Chungui Tian

School of Chemistry and Materials Science, Heilongjiang University, Harbin 150080, China

ARTICLE INFO

Article history:
Received 26 February 2008
Received in revised form 16 April 2008
Accepted 17 April 2008
Available online 24 April 2008

Keywords:
Photocatalyst
Photocatalytic activity
Crystallinity
Phase stability

ABSTRACT

Superior photoactive TiO_2 nanopowders with high crystallinity and large surface area were synthesized by a hydrothermal process in the presence of cetyltrimethylammonium bromide and a post-treatment with ammonia. The prepared photocatalysts were characterized by X-ray diffraction (XRD), Raman spectroscopy, N_2 adsorption–desorption, transmission electron microscopy (TEM), X-ray photoelectron spectroscopy (XPS), Fourier transform infrared spectroscopy (FTIR), UV–vis diffuse reflectance spectra (DRS) and surface photovoltage spectroscopy (SPS). The prepared nanocrystallites were highly resistant to thermal sintering, and the calcinations up to 900 °C were shown to enhance the crystallinity of the anatase phase without any rutile phase and the separation rate of photoinduced charges of TiO_2 particles. It remained as large as 196 and 125 m^2/g even after calcinations at 700 and 800 °C, respectively. The photocatalytic activity of prepared photocatalysts was obviously higher than that of commercial Degussa P25 on the photodegradation of methylene blue and phenol in water under ultraviolet-light irradiation, and the sample calcined at 800 °C afforded the highest photocatalytic activity.

1. Introduction

Harmful pollutants, especially dyes and aromatic hydrocarbons, are typical pollutants emitted from industrial and domestic activities [1]. Among the technologies developed for the treatment of harmful pollutants, the photocatalytic oxidation process using heterogeneous photocatalysis is regarded as a promising technology to decompose harmful pollutants to final non-toxic products. Titanium dioxide has been proved to be a very efficient photocatalyst for the degradation of harmful pollutants in water and air because of its high stability, nontoxicity and inexpensiveness [2]. However, low photocatalytic activity is one of the major factors keeping it from large-scale applications. Thus, it is crucial to improve the photocatalytic activity of TiO_2. The photocatalytic activity of TiO_2 system depends on its intrinsic properties, such as crystal phase, crystallinity and specific surface area [3–5]. Furthermore, the catalytic activity of TiO_2 also depends strongly on electron–hole separation, and the key of the photocatalytic process is to inhibit the recombination of electron and hole [6]. It is widely accepted that the anatase phase of titania is a relatively ideal photocatalytic material among its three crystalline phases [7]. In addition, it has been known that anatase powders with small fraction of rutile or brookite phase, show enhanced photocatalytic activity compared to pure anatase powders due to the electron and hole transfer between the two phases [8,9]. Yu et al. have reported the result that anatase–brookite composite nanocrystals synthesized by a sonochemical sol–gel method show a very high photocatalytic activity [10].

It is generally accepted that a good crystallinity is required to reduce the formation of electron traps, which can less recombination centers of photogenerated electrons and holes [11]. Alternative synthetic methods, with respect to the classical high temperature calcinations are, therefore, sought to comply with the demanding, divergent material requirements [12,13]. In fact, the introduction of high temperature stages, to promote crystallinity, frequently gives rise to particle agglomeration with severe loss of effective surface area and phase transformation [14]. Therefore, many attempts have been made to inhibit grain growth and retard phase transformation at elevated temperatures by the use of metal oxide dopants [15,16]. However, the presence of secondary impurity phases at high temperature is the main disadvantages, which could keep it from potential applications [17].

Recently, Cassiers et al. prepared mesoporous titania using evaporation-induced self-assembly method with a subsequent treatment with ammonia [18]. The obtained mesoporous titania samples exhibit a high surface area. But in that method, amorphous phase remained in the titania wall and was apt to transform into rutile, two aspects do not enhance photocatalytic activity. In addition, there is no study available in the literature on the effect of ammonia treatment on high temperature phase stability of anatase and photocatalytic activity.

* Corresponding author. Tel.: +86 451 86608458; fax: +86 451 86673647.
E-mail address: fuhg@vip.sina.com (H. Fu).

0304-3894/$ – see front matter © 2008 Elsevier B.V. All rights reserved.
doi:10.1016/j.jhazmat.2008.04.065

In our study, porous titania particles were prepared via hydrothermal process starting from preformed TiO_2 nanocrystals using cetyltrimethylammonium bromide (CTAB) as templates and a post-treatment with ammonia. The phase transformation during heat treatment was investigated by X-ray diffraction (XRD) and Raman spectroscopy. The study showed that a major anatase phase can be retained even at 900 °C without appearance of rutile by the post-treatment. The prepared TiO_2 photocatalysts have the characteristics of high crystallinity, large surface area and bicrystalline (anatase and brookite) framework. They exhibit better photoactivity than Degussa P25 on the degradation of methylene blue and phenol in water under UV irradiation.

2. Experimental

2.1. Preparation of catalysts

A mixture of 40 ml tetrabutyl titanate (TBT) and 10 ml ethanol was slowly dropped into the solution containing 250 ml deionized H_2O and 2 ml hydrochloric acid in an ice bath under vigorously stirring. After refluxing for 4 h at 70 °C, the resulting mixture solution of TiO_2 nanocrystals was then cooled to room temperature. A solution of CTAB and NH_4OH (7%) was then slowly dropped into the above mixture solution under stirring, the molar ratio of TBT:CTAB is 1:0.12, and pH was 10. After stirring for 1 h at room temperature, the mixture was transferred to a Teflon-lined autoclave for hydrothermal treatment at 180 °C for 8 h. Afterwards, the sample was treated with NH_4OH basic water for 48 h in a reflux system. One gram of sample was treated with 30 ml of the basic water, the pH was kept constant at 9–10 by the drop addition of NH_4OH (28%) [18]. The resulting powder was calcined in air at 400–900 °C for 4 h to improve crystallinity with a heating rate of 1 °C min^{-1}. The products were denoted as TiO_2–NH_3-*T*. For comparison, TiO_2 without post-treatment was also prepared and denoted as TiO_2-*T*, where *T* refers to the calcination temperature.

2.2. Characterization of the samples

XRD patterns were carried out on a Rigaku D/MAX X-ray diffractometer, using Cu Kα radiation with $\lambda = 0.15406$ nm. The accelerating voltage and applied current were 20 kV and 20 mA, respectively. Raman measurements were made operating at 457.9 nm by a Jobin–Yvon HR800 spectrometer with an Ar ion laser beam. After samples had been vacuum-dried at 200 °C overnight, nitrogen adsorption–desorption isotherms were collected on a AUTOSORB-1 (Quantachrome Instruments) nitrogen adsorption apparatus at 77 K. The pore-size distribution plots were obtained by the Barret–Joyner–Halenda (BJH) model. Transmission electron microscopy (TEM) and select area electron diffraction (SAED) were recorded on a JEOL 2010 microscope with a 200 kV accelerating voltage. High-resolution transmission electron micrograph (HRTEM) was obtained by employing a FEI TECNAI G2 S-TWIN with a 200 kV accelerating voltage. X-ray photoelectron spectroscopy (XPS) measures were performed with Thermo ESCALAB 250. The surface photovoltage spectroscopy (SPS) measurement of the samples was carried out with a home-built apparatus that had been described elsewhere [19,20]. The raw SPS data were normalized using the illuminometer (Zolix UOM-1S, made in China). UV–vis diffuse reflectance spectra (DRS) were determined by a UV–vis spectrophotometer (Shimadzu UV-2550). The surface-adsorbed water and hydroxyl groups on the photocatalysts were studied by Fourier transform infrared spectroscopy (FTIR, PerkinElmer spectrum one).

2.3. Photocatalytic experiments

The photodegradation experiments were performed in a slurry reactor containing 20 ml of a 10 mg l^{-1} solution of methylene blue (MB) and 0.05 g of catalyst. The reaction solution was kept in the dark under stirring for 30 min, then the solution was irradiated with a 20 W UV lamp with a maximum emission at approximately 365 nm, and the average light intensity striking the TiO_2 powder was about 1000 μW cm^{-2}, as measured by a UV radiometer (made in the Photoelectric Instrument Factory of Beijing Normal University). The concentrations of MB solutions before and after UV irradiation were determined by a UV–vis spectrophotometer (Shimadzu UV-2550) from the absorbance at 664 nm. Total organic carbon (TOC) was measured via a TOC-analyzer (Shimadzu 5000A) equipped with an auto-sampler (ASI-5000).

The photocatalytic activities of the samples (50 mg) were also evaluated by the degradation of phenol in aqueous solution (20 ml, with initial concentration of 50 mg l^{-1}). For comparison, an experiment was carried out with a Degussa P25 catalyst under the same condition. The sample was magnetically stirred for 30 min to establish an adsorption–desorption equilibrium prior to UV irradiation. Afterward, the solution was irradiated with a 20 W UV lamp with a maximum emission at approximately 365 nm, and the average light intensity striking the TiO_2 powder was about 1000 μW cm^{-2}, as measured by a UV radiometer (made in the Photoelectric Instrument Factory of Beijing Normal University). Oxygen flow was employed in all experiments as an oxidant. Experiments were performed for 120 min. The sample was subjected to filtration through a 0.2-μm syringe filter (Millipore, cellulose acetate membrane) to remove particles before HPLC analysis of phenol concentration. The column used was a Shimadzu 250 × 4.6 (250-mm length × 4.6-mm diameter), packed with RP-C18. A mixture of methanol (70%, v/v) and deionized water was used as the mobile phase at a flow rate of 1.0 ml min^{-1}. An aliquot of 20 μl of the sample was injected and analyzed at a wavelength of 270 nm with an UV detector (Shimadzu SPD-10A). The chromatographic areas were converted to concentration values using calibration curves based on pure compound.

3. Results and discussion

3.1. XRD and Raman analysis

XRD was used to calculate the phase content and investigate the changes of phase structure of the as-prepared TiO_2 powders before and after treatment. Raman spectroscopy was also introduced to investigate various phases of titanium dioxide because of its much more sensitive technique for the detection of nanosized crystalline domains compared with XRD. From Fig. 1, it can be seen that the as-prepared TiO_2 after hydrothermal process is composed of nanoparticles with crystalline structure. Moreover, NH_3-treatment and calcination temperature obviously influence the crystallization and phase composition of the TiO_2 powders. The weight percentage of each crystal phase can be calculated from individual diffraction peaks on the basis of formulas reported in the literature [21]. It was found that when the calcination temperature was below 600 °C, the TiO_2-*T* samples displayed dominantly anatase phase and a small amount of brookite, which could be obviously seen from the corresponding Raman spectra (Fig. 2(a)), when the calcination temperature was above 600 °C, brookite phase disappeared, anatase to rutile phase transformation and subsequent crystal growth occurred. However, all the NH_3-treated samples calcined at different temperatures have a biphase composition of anatase and brookite. With increasing calcination temperature

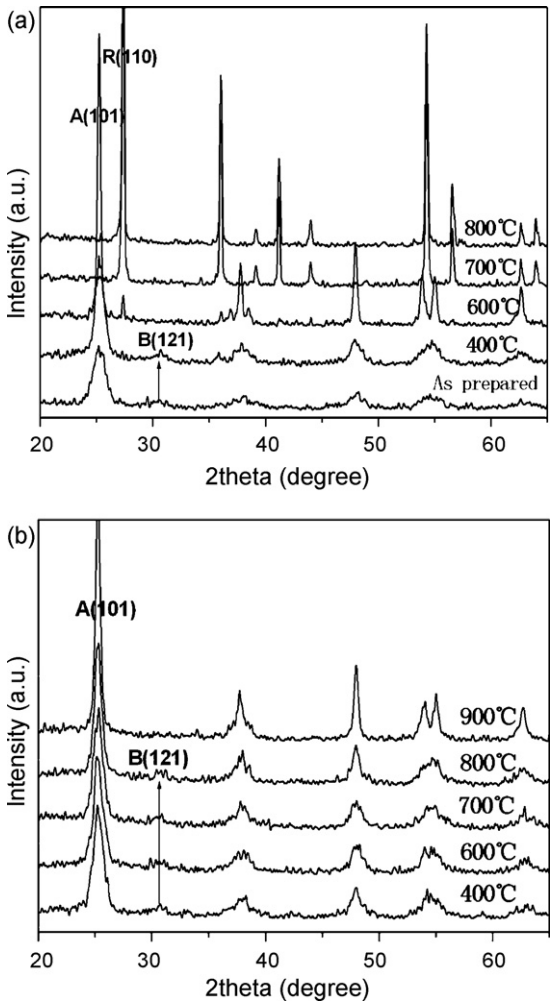

Fig. 1. Wide-angle XRD patterns of TiO_2-*T* (a) and TiO_2–NH_3-*T* (b) samples calcined at different temperatures. The peaks marked A, R, and B represent the anatase, rutile and brookite phase, respectively.

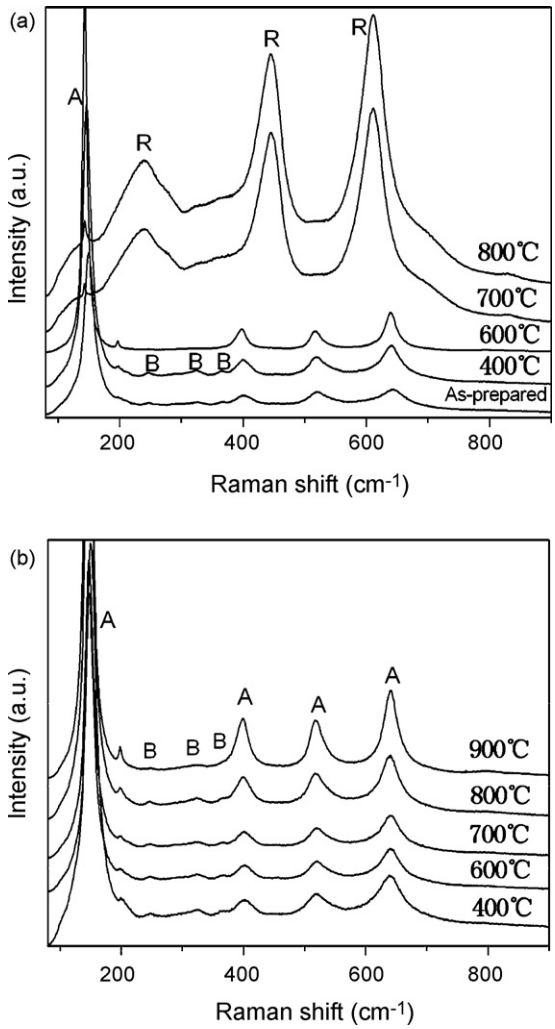

Fig. 2. Raman spectra of TiO_2-*T* (a) and TiO_2–NH_3-*T* (b) samples calcined at different temperatures.

from 400 to 900 °C, the content of brookite gradually decreased. At 900 °C, we cannot find the (1 2 1) diffraction peak of brookite from XRD. But from corresponding Raman spectra (Fig. 2(b)), we can find three obvious peaks at 247, 318 and 366 cm^{-1}, which are attributed to A_{1g}, B_{1g} and B_{2g} vibration modes for the brookite phase of TiO_2 [22]. So there still exist a trace brookite, and no rutile phase is observed at 900 °C. It means that the anatase to rutile phase transformation has therefore, been found to be effective in extending by at least 300 °C without using any metal oxide dopants. Moreover, all the diffraction peaks of anatase become sharper and intenser, which hints the gradual improvement of crystallinity. The crystal sizes of TiO_2–NH_3-*T* samples calcined between 400 and 900 °C are in the range of 6.5–15.2 nm according to the Scherrer's equation (Table 1), which is much smaller than that of the corresponding TiO_2-*T* sample. This indicates that post NH_3-treatment can effectively suppress grain growth and phase transformation upon high temperature calcination. The significant effect on the phase stability may be attributed to the presence of impure residues by restricting direct contact of grains [23], and relative small grain size may be another reason [11], so the phase

Table 1
Physicochemical properties of the obtained TiO_2 in comparison with those of P25

Sample	Phase content (%)	S_{BET} ($m^2\ g^{-1}$)	Crystalline size (nm)	Pore volume ($ml\ g^{-1}$)	Mean pore size (nm)
As-prepared	A (72) + B (28)	120	A (6.2), B (5.1)	0.28	2.1
TiO_2-400	A (74) + B (26)	146	A (8.8), B (6.8)	0.36	2.4
TiO_2-600	A (91) + R (9)	36	A (18.4), R (25.4)	–	–
TiO_2-700	A (8) + R (92)	7	A (25.3), R (33.1)	–	–
TiO_2-800	R (100)	1.6	R (41.2)	–	–
TiO_2–NH_3-400	A (73) + B (27)	280	A (6.5), B (5.7)	0.48	2.2
TiO_2–NH_3-600	A (76) + B (24)	225	A (7.1), B (6.2)	0.42	2.4
TiO_2–NH_3-700	A (79) + B (21)	196	A (7.9), B (6.7)	0.34	2.6
TiO_2–NH_3-800	A (82) + B (18)	125	A (9.7), B (8.5)	0.22	2.9
TiO_2–NH_3-900	A (94) + B (6)	42	A (15.2), B (13.1)	–	–
P25	A (80) + R (20)	50	A (22), R (28)	–	–

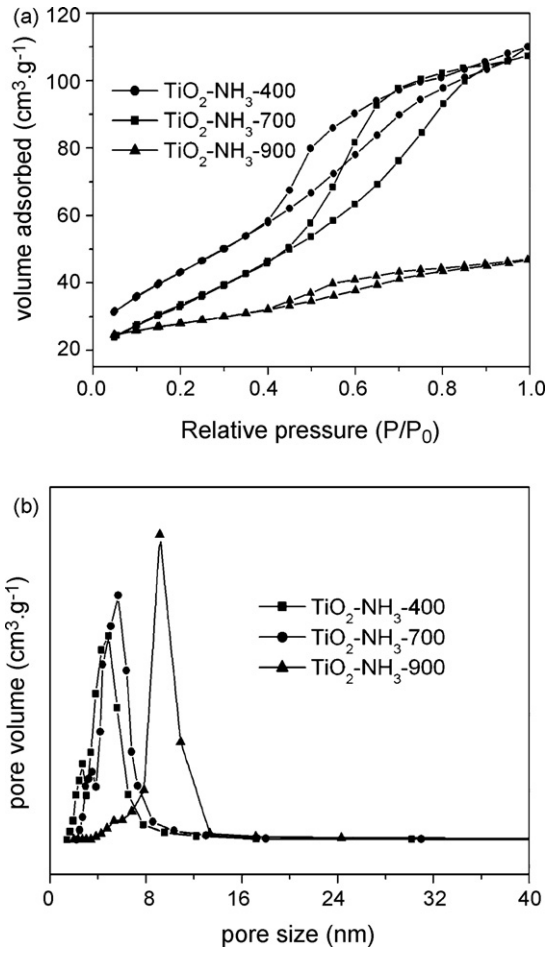

Fig. 3. N_2 adsorption–desorption isotherms (a) and corresponding pore-size distribution plots (b) of TiO_2–NH_3-*T* samples calcined at 400, 700 and 900 °C.

transformation was significantly inhibited even at 900 °C in spite of no impurity at this temperature. Small titania particles with high crystallinity are very beneficial in enhancing the photocatalytic activity.

3.2. BET surface areas and pore structure analysis

N_2 adsorption–desorption isotherms of TiO_2–NH_3-*T* samples calcined at 400, 700 and 900 °C are presented in Fig. 3(a). It can be seen that all the isotherms, except for that of TiO_2–NH_3-900, are type VI according to the IUPAC classification [24], indicative of a solid porous structure. With increasing calcination temperature, the hysteresis loops in the N_2 adsorption–desorption isotherms shifted to the region of higher relative pressure, and the volume of pore gradually decreased. Fig. 3(b) shows the corresponding BJH pore-size distribution of the TiO_2 powders calcined at different temperatures. All the powders except for the sample calcined at 900 °C show bimodal pore-size distributions, the former ones come from fine intra-aggregated pores (2–3 nm), and the latter from larger inter-aggregated pores (4–10 nm) originating from hard aggregates in the powders [25]. With increasing calcination temperatures, the pore-size distribution peak shifted to right, and the intra-particle pore-size peak became weak. The changes could be ascribed to a partial collapse of the intra-aggregated pores and the increase of crystallization. The specific surface area of the TiO_2-400 was found to be 146 $m^2\,g^{-1}$. After calcination at 700 °C, the surface area decreased drastically to 7 $m^2\,g^{-1}$, which was due to the collapse of the porous framework. The TiO_2–NH_3-*T* samples, however, had much higher surface area and larger pore volumes than the corresponding TiO_2-*T* ones (see Table 1). The specific surface area of TiO_2–NH_3-400 was 280 $m^2\,g^{-1}$, it remained as large as 196 and 125 $m^2\,g^{-1}$ even after calcinations at 700 and 800 °C, respectively. Therefore, it is easy to note that NH_3-treatment can stabilize the framework of porous TiO_2.

3.3. TEM analysis

The TEM images of the prepared TiO_2–NH_3-*T* samples calcined at 400, 800 and 900 °C are shown in Fig. 4. All the samples, except for the sample calcined at 900 °C, show similar porous characteristics. The morphologies of pores and particles are not changed significantly upon heating up to 800 °C, which means that the collapse and aggregate do not occur drastically upon calcinations. After calcination at 900 °C, the powders change into nonporous particles with mean particles size of 15 nm. The gradual increase of crystallinity can be further confirmed by the selected-area electron diffraction patterns inserted in Fig. 4(a) and (b), revealing diffraction rings typical for a crystalline powder due to the absence of an amorphous halo. The results were in general agreement with the XRD determination. The HRTEM image in Fig. 4(c) shows the micrograph of TiO_2–NH_3-800, the inset is the Fourier transform of the HRTEM image. It was found that the pore walls (indicated by the white arrows) consisted of aggregated nanocrystals, implying their excellent crystallinity as also evidenced by the well resolved lattice fringes, where the *d*-spacing of 0.352 nm corresponds to the (1 0 1) plane of the anatase lattice.

3.4. XPS and FTIR analysis

XPS measurements have been carried out to determine N and O states in the photocatalyst. Fig. 5(a) shows the N 1s XPS spectra of TiO_2-700, TiO_2–NH_3-800 and TiO_2–NH_3-900. For the TiO_2–NH_3-800, a peak appeared at 400.0 eV, and this peak was ascribed to the N atoms from adventitious N–H, O–N, or N-containing organic compounds adsorbed on the surface [26,27]. However, there was no indication of Ti–N bond formation (396 eV) [28]. However, for TiO_2-700 and TiO_2–NH_3-900 powders, no peak was observed in the N 1s XPS spectra. The results suggested that there still remained some impure residues in TiO_2–NH_3-800 powders, but there was no impurity in the TiO_2–NH_3-900 and TiO_2-700 powders. The presence of impure residues may restrict direct contact of grains and play a positive role in inhibiting the crystal growth and phase transformation. Fig. 5(b) shows the XPS spectra of the O 1s region taken on the surface of TiO_2-*T* and TiO_2–NH_3-*T* samples calcined at 800 °C. The O 1s region of the calcined TiO_2-*T* is composed of a single peak at 529.8 eV, corresponding to the Ti–O in TiO_2. However, the broad O 1s region of the calcined TiO_2–NH_3-*T* has two obvious peaks, which are Ti–O in TiO_2 and hydroxyl groups, respectively. The binding energy of the Ti–O in TiO_2 is 529.3 eV with 67.4% in contribution. For the hydroxyl groups, the binding energy is 531.4 eV with 32.6% in contribution. The FT-IR spectra of TiO_2-*T* and TiO_2–NH_3-*T* calcined at 800 °C are shown in Fig. 6. It is believed that the broad peak at 3400 and the peak at 1650 cm^{-1} correspond to the surface adsorbed water and hydroxyl groups. Obviously, the calcined TiO_2–NH_3-*T* has more surface-adsorbed water and hydroxyl groups than the calcined TiO_2-*T*, which confirms the XPS results. This can be attributed to the larger surface area of the calcined TiO_2–NH_3-*T*. Porous TiO_2 of larger surface area can offer more active sites to adsorb water and hydroxyl groups.

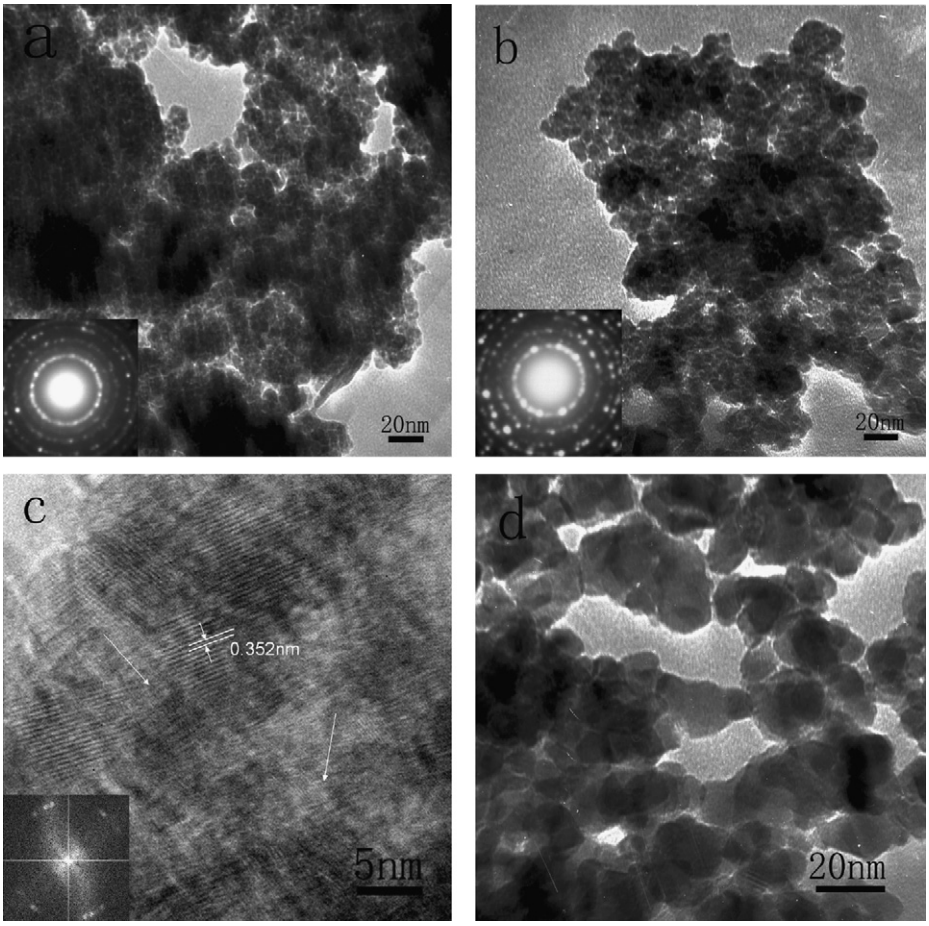

Fig. 4. TEM images of TiO_2–NH_3-*T* samples calcined at 400 °C (a), 800 °C (b) and (c), 900 °C (d).

3.5. UV–vis diffuse reflectance spectra analysis

Fig. 7(a) shows the UV–vis diffuse reflectance of TiO_2–NH_3-*T* samples together with Degussa P25. It can be seen that TiO_2–NH_3-*T* samples exhibit a systemic "red-shift" in absorption edges with the increase of calcination temperature. The direct band gap energy can be estimated from a plot of $(\alpha h\nu)^{1/2}$ versus photon energy ($h\nu$) as shown in Fig. 7(b). The intercept of the tangent to the plot will give a good approximation of the band gap energy for the TiO_2 [29]. The estimated band gap energies are 3.21, 3.20, 3.19, 3.17 and 3.15 eV for TiO_2–NH_3-*T* with the increase of calcination temperature from 400 to 900 °C, all data is larger than that of Degussa P25 (E_g = 3.12 eV). Quantum size effect and the existence of brookite might be responsible for the larger band gap of the TiO_2–NH_3-*T* samples [30]. Moreover, TiO_2–NH_3-*T* samples exhibit higher absorption in the ultraviolet light range than that of Degussa P25, which would be beneficial for photodegradation of organic pollutants under UV irradiation.

3.6. SPS analysis

The SPS technique can provide a rapid, non-destructive test of semiconductor solid surface property, and is also a very effective way to study the separation and transfer behavior of photoinduced charge carriers at a surface or interface [19,20]. Fig. 8 shows the SPS responses of the obtained TiO_2 nanoparticles calcined at different temperatures, the SPS peaks appear at about 345 nm, which can be attributed mainly to the electron transition from the valence band to conduction band (O 2p → Ti 3d) on the basis of TiO_2 band structure [31]. And as the thermal treatment temperature rises, there is a significant increase in the intensity of SPS spectra, indicating that the recombination rate of photoexcited electrons and holes was decreased gradually by eliminating as much as possible the recombination process occurring in the crystal defects of the structure. This can be reasonably explained by means of the results of XRD and Raman measurements, the increase of crystallinity leads to the reduction of crystal defects of the structure, which would result into the decrease in the recombination chance of photoinduced carriers, so that the separation rate of photoinduced electron–hole pairs can be improved.

3.7. Photocatalytic activity

The photocatalytic activities of our synthesized TiO_2–NH_3-*T* photocatalysts and commercial Degussa P25 were evaluated according to their photodegradation rates to MB in aqueous solution. The degree of adsorption in a dark condition was also evaluated by stirring suspensions of MB (10 mg l^{-1}) in TiO_2 (2.5 g l^{-1}) for 30 min. The adsorbed MB is 10.5%, 10.1%, 9.9%, 9.1%, 7.7%, and 8.5% in the suspensions of TiO_2–NH_3-400, TiO_2–NH_3-600, TiO_2–NH_3-700, TiO_2–NH_3-800, TiO_2–NH_3-900, and P25, respectively. The adsorption data showed that, except for TiO_2–NH_3-900, the adsorption capability in MB on obtained catalysts was larger than that on Degussa P25, which is mainly due to the high specific surface area and large pore volume of the formed structure. The time course of the photocatalytic degradation of MB (10 mg l^{-1}) on UV

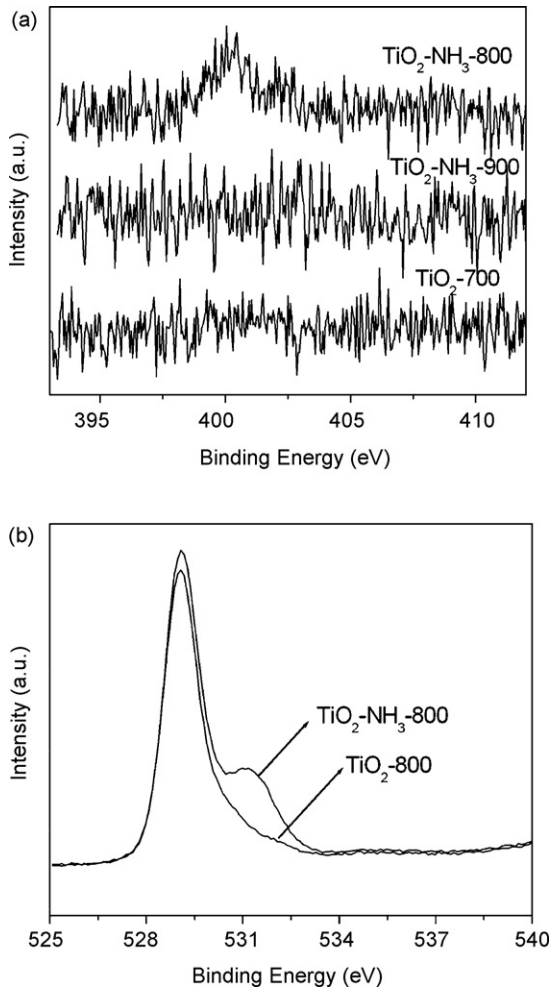

Fig. 5. X-ray photoelectron spectra of N 1s (a) for the samples of TiO_2-700, TiO_2–NH_3-800 and TiO_2–NH_3-900 and O 1s (b) for the samples of TiO_2–NH_3-800 and TiO_2-800.

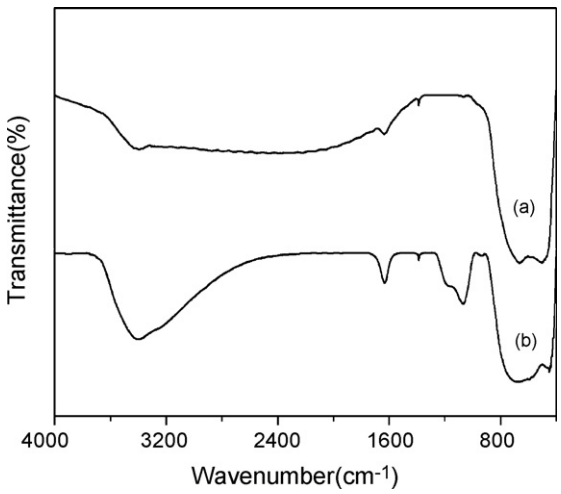

Fig. 6. FT-IR spectra of TiO_2-*T* and TiO_2–NH_3-*T* calcined at 800 °C (a), and (b) represent TiO_2-*T* and TiO_2–NH_3-*T*, respectively.

light irradiated catalysts is shown in Fig. 9. It can be seen that all TiO_2–NH_3-*T* samples showed higher activity than Degussa P25. Photocatalytic degradation of MB at low concentration followed pseudo-first-order kinetics. We have derived the apparent reaction rate constants for the photodegradation of MB from the linear slope of the relationship between $\ln(c/c_0)$ and $k_a t$, where c_0 and c are the concentrations of initial solution and after t (min) of irradiation, respectively. In addition, the photodecomposition of various initial concentrations of MB, such as 20 and 30 mg l^{-1}, was also studied in the presence of fixed catalyst dose. The calculated data for pseudo-first-order rate constants (k_a) at different MB concentrations are shown in Table 2. It can be observed that, all the prepared catalysts exhibited higher k_a value than Degussa P25 under the same initial MB concentration. For the same catalyst, the rate constant value was found to decrease with the increase of initial MB concentration. This is mainly because of the fact that, at higher concentration of substrate, the light absorbed by the substrate is more than that of the catalyst, but not effective in bringing the photodegradation. For a fixed catalyst dose, the active sites remain the same, the number of substrate ions accommodated in the interlayer space increases, so there is a decrease in the photocatalytic degradation.

To examine the mineralization of MB solution, TOC removal was also studied, as shown in Fig. 10. It was found that at 60 min the TOC removals reached 67%, 78%, 92%, 96%, 86%, and 58% in the suspensions of TiO_2–NH_3-400, TiO_2–NH_3-600, TiO_2–NH_3-700, TiO_2–NH_3-800, TiO_2–NH_3-900, and Degussa P25, respectively. The values of TOC conversions reflected well the conclusions drawn above about the catalytic performances.

Based on above experiment data, apart from dark adsorption capacity, all the TiO_2–NH_3-*T* samples have better degradation and mineralization ability than Degussa P25. Their high photocatalytic activity might be understood by considering the factors of large specific surface area, low recombination rate of electrons and holes, and large band gap, as described above. In addition, heterojunction microstructure between anatase and brookite can increase charge separation efficiency, and therefore, increase the photocatalytic activity [32].

Moreover, the photocatalytic activity of the TiO_2–NH_3-*T* sample increases apparently with increasing calcination temperature (*T*) in the range of 400 °C ≤ *T* ≥ 800 °C. Noticeably, the sample (TiO_2–NH_3-800) calcined at 800 °C shows, among the TiO_2–NH_3-*T* samples, the highest photocatalytic activity. When the calcination temperature continuously increases, the photocatalytic activity begins to fall down inversely. It was found that, in response to the gradual

Table 2
Rate constant values for the photodegradation of MB with different initial concentrations on TiO_2–NH_3-*T* samples calcined at different temperatures and Degussa P25 in the presence of fixed catalyst dose (50 mg l^{-1})

Photocatalysts	Kinetic constant, K_a (min^{-1})		
	Concentration (10 mg l^{-1})	Concentration (20 mg l^{-1})	Concentration (30 mg l^{-1})
TiO_2–NH_3-400	0.1353	0.0902	0.0512
TiO_2–NH_3-600	0.1546	0.1030	0.0565
TiO_2–NH_3-700	0.1702	0.1105	0.0636
TiO_2–NH_3-800	0.1729	0.1152	0.0748
TiO_2–NH_3-900	0.1645	0.1067	0.0601
P25	0.1271	0.0847	0.0476

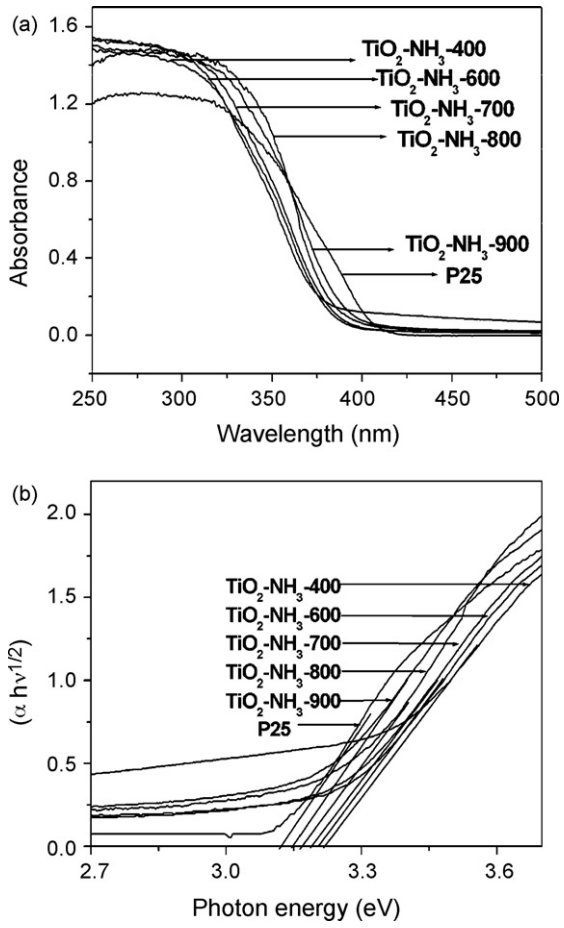

Fig. 7. UV–vis diffuse reflectance spectra (a) and plots of $(\alpha h\nu)^{1/2}$ vs. photon energy ($h\nu$), and (b) for TiO_2–NH_3-*T* samples calcined at different temperatures and Degussa P25.

reduction of specific surface area, the separation rate of photoinduced electron–hole pairs gradually improves with the increase of calcination temperature according to the SPS response because of the gradual increase of crystallinity. The cooperative effect of these properties leads to the best photocatalytic performance at 800 °C. After the calcination at 900 °C, in spite of having higher separation rate of photoexcited carriers, the sample showed a slightly reduced

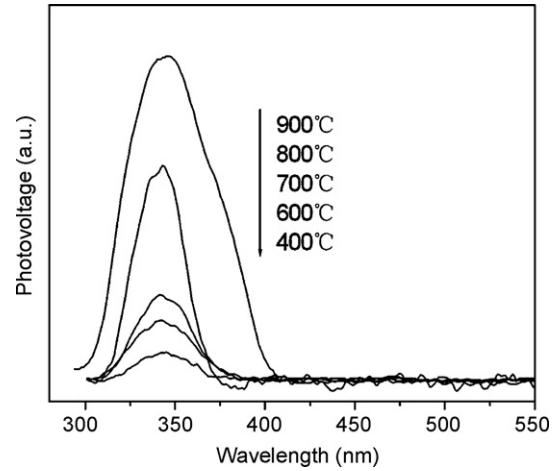

Fig. 8. SPS responses of TiO_2–NH_3-*T* samples calcined at different temperatures.

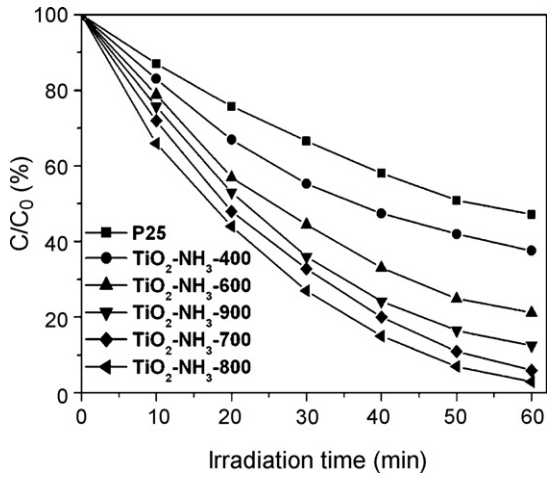

Fig. 9. The profiles of MB (10 mg l^{-1}) degradation with a catalyst amount of 2.5 g l^{-1} with TiO_2–NH_3-*T* and Degussa P25 under UV irradiation.

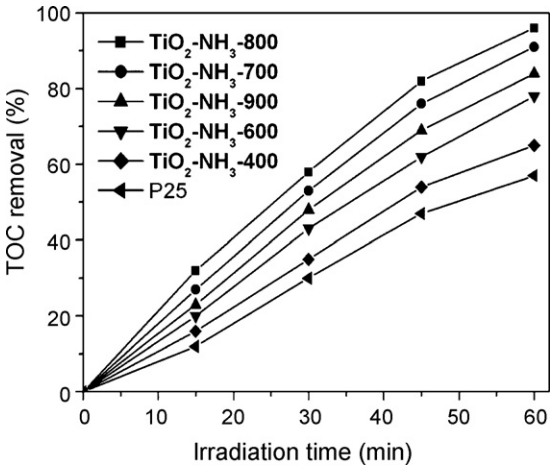

Fig. 10. The profiles of TOC removals for the photodegradation of MB (10 mg l^{-1}) in different aqueous TiO_2 suspensions (2.5 g l^{-1}) under UV irradiation.

photoactivity due to the extensive decrease of specific surface area (42 m^2 g^{-1}) and the great growth of the sample particles.

In this paper, we also investigated the photocatalytic activity of TiO_2–NH_3-*T*, TiO_2-*T* and Degussa P25 (see Fig. 11) on the degradation of phenol. It was worth noting that all TiO_2–NH_3-*T* samples

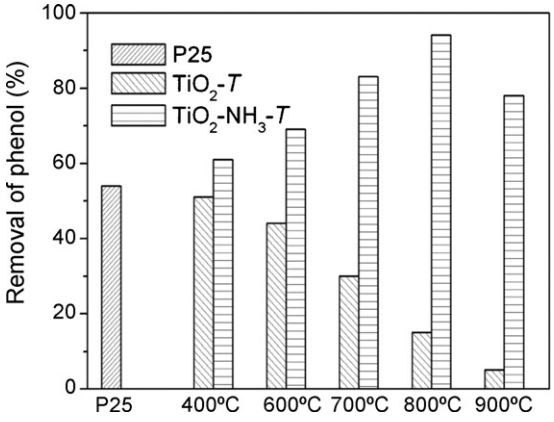

Fig. 11. Photocatalytic degradation of phenol (50 mg l^{-1}) on TiO_2–NH_3-*T* and TiO_2-*T* samples calcined at different temperatures as well as the Degussa P25 for comparison.

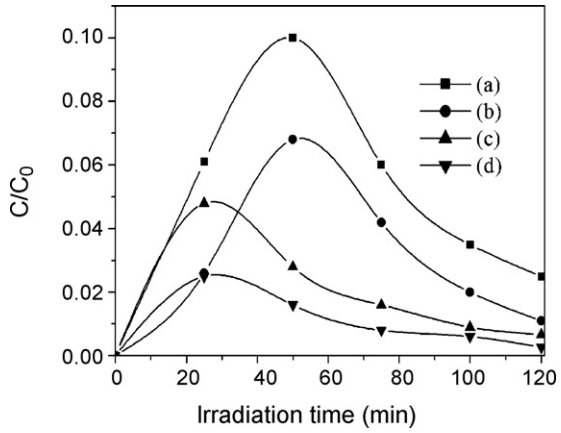

Fig. 12. Variation of the concentration of the intermediates formed during the degradation of phenol with a different samples: (a) catechol, Degussa P25; (b) hydroquinone, Degussa P25; (c) catechol, TiO_2–NH_3-800; and (d) hydroquinone, TiO_2–NH_3-800.

showed higher activity than Degussa P25 and the overall trend of photoactivity was very similar to that on the degradation of MB. Interestingly, it was observed that the calcined TiO_2–NH_3-*T* had better photocatalytic activity than the calcined TiO_2-*T*. This can be explained that TiO_2–NH_3-*T* has smaller particle size, larger surface area and porous structure compared with TiO_2–T. Smaller TiO_2 particles are beneficial for the more effective photogenerated carriers separation, porous TiO_2 of larger surface area can has a larger number of hydroxide ions on its surface, and exhibit a higher photocatalytic reaction rate [33].

HPLC analysis was also used to detect and quantitate the main intermediates of the photocatalytic degradation of phenol. During all the photocatalytic processes, catechol and hydroquinone were detected as main reaction intermediates, confirming that the mechanisms for the degradation of phenol are similar in the presence of Degussa P25 and the prepared photocatalysts. The variation of the concentration of the intermediates (catechol and hydroquinone) increases initially and then decreases. Moreover, for the TiO_2–NH_3-*T* samples, for example, TiO_2–NH_3-800, the quantity of aromatic intermediates formed when phenol is degraded by TiO_2–NH_3-800 is lower than that of aromatic intermediates formed when phenol is degraded by Degussa P25 as shown in Fig. 12. The results indicate that the total disappearance rate of phenol and its intermediates is faster during the phenol degradation by the prepared TiO_2–NH_3-*T* catalysts compared with that of Degussa P25.

4. Conclusions

Highly active porous biphase TiO_2 nanopowders were synthesized by a hydrothermal process and a post-treatment with ammonia. The introduction of NH_3-treatment considerably inhibits the undesirable grain growth and phase transformation during calcination. The photocatalytic activity of the as-prepared TiO_2–NH_3-*T* samples was obviously higher than that of Degussa P25 and TiO_2-*T* samples for the photocatalytic degradation of methylene blue and phenol. With increasing the calcination temperature up to 800 °C, the photocatalytic activity of TiO_2 photocatalysts increased gradually, the sample calcined at 800 °C showed the highest photocatalytic activity because of the synergetic effects of large surface area, high crystallinity and separation rate of photoexcited carriers, and heterojunction microstructure between anatase and brookite. After calcination at 900 °C, the sample showed reduced activity due to the extensive decrease of specific surface area and the sintering growth of the sample particles.

Acknowledgments

The work was supported by the Key Program Projects of National Natural Science Foundation of China (No. 20431030), the National Natural Science Foundation of China (No. 20501007, No. 20671032), the Program for New Century Excellent Talents in University (NCET-04-0341).

References

[1] S.C. Wilson, V. Burnett, K.S. Waterhouse, K.C. Jones, Volatile organic compounds in digested United Kingdom sewage sludges, Environ. Sci. Technol. 28 (1994) 259–266.
[2] D.F. Ollis, E. Pelizzetti, N. Serpone, Photocatalyzed destruction of water contaminants, Environ. Sci. Technol. 25 (1991) 1522–1529.
[3] Z. Ding, G.Q. Lu, P.F. Greenfield, Role of the crystallite phase of TiO_2 in heterogeneous photocatalysis for phenol oxidation in water, J. Phys. Chem. B 104 (2000) 4815–4820.
[4] Y.Q. Wang, X.H. Tang, W. Huang, Y. Yin, R. Hacohen, A. Gedanken, Sonochemical synthesis of mesoporous titanium oxide with wormhole like framework structures, Adv. Mater. 12 (2000) 1183–1186.
[5] P. Pucher, M. Benmami, R. Azouani, G. Krammer, K. Chhor, J.-F. Bocquet, A.V. Kanaev, Nano-TiO_2 sols immobilized on porous silica as new efficient photocatalyst, Appl. Catal. A: Gen. 332 (2007) 297–303.
[6] A. Fujishima, T.N. Rao, D.A. Tryk, Titanium dioxide photocatalysis, J. Photochem. Photobiol. C: Photochem. Rev. 1 (2000) 1–21.
[7] J. Ovenstone, K. Yanagisawa, Effect of hydrothermal treatment of amorphous titania on the phase change from anatase to rutile during calcinations, Chem. Mater. 11 (1999) 2770–2774.
[8] C.H. Deanna, G.A. Alexander, A.G. Kimberly, Explaining the enhanced photocatalytic activity of Degussa P25 mixed-phase TiO_2 using EPR, J. Phys. Chem. B 107 (2003) 4545–4549.
[9] T. Ozawa, M. Iwasaki, H. Tada, T.K. Akita, S.I. Tanaka, Low-temperature synthesis of anatase–brookite composite nanocrystals: the junction effect on photocatalytic activity, J. Colloid Interface Sci. 281 (2005) 510–513.
[10] J.G. Yu, J.C. Yu, W. Ho, L.Z. Zhang, Preparation of highly photocatalytic active nano-sized TiO_2 particles via ultrasonic irradiation, Chem. Commun. 19 (2001) 1942–1943.
[11] H. Zhang, J.F. Banfield, Thermodynamic analysis of phase stability of nanocrystalline titania, J. Mater. Chem. 8 (1998) 2073–2076.
[12] D.T. On, A simple route for the synthesis of mesostructured lamellar and hexagonal phosphorus-free titania (TiO_2), Langmuir 15 (1999) 8561–8564.
[13] V.F.J. Stone, R. Davis, Synthesis, characterization, and photocatalytic activity of titania and niobia mesoporous molecular sieves, Chem. Mater. 10 (1998) 1468–1474.
[14] S.H. Elder, Y. Gao, X. Li, J. Liu, D.E. McCready, C.F. Windisch, Preparation of stable anatase-type TiO_2 and its photocatalytic performance, Chem. Mater. 10 (1998) 3140–3145.
[15] K.T. Ranjit, I. Willner, S.H. Bossmann, A.M. Braun, Lanthanide oxide-doped titanium dioxide photocatalysts: novel photocatalysts for the enhanced degradation of *p*-chlorophenoxyacetic acid, Environ. Sci. Technol. 35 (2001) 1544–1549.
[16] J. Zhang, M.J. Li, Z.C. Feng, J. Chen, C. Li, UV Raman spectroscopic study on TiO_2. I. phase transformation at the surface and in the bulk, J. Phys. Chem. B 110 (2006) 927–935.
[17] I.P. Parkin, R.G. Palgrave, Self-cleaning coatings, J. Mater. Chem. 15 (2005) 1689–1695.
[18] K. Cassiers, T. Linssen, M. Mathieu, Y.Q. Bai, H.Y. Zhu, P. Cool, E.F. Vansant, Surfactant-directed synthesis of mesoporous titania with nanocrystalline anatase walls and remarkable thermal stability, J. Phys. Chem. B 108 (2004) 3713–3721.
[19] L.Q. Jing, Z.L. Xu, J. Shang, X.J. Sun, W.M. Cai, H.G. Fu, Review of surface photovoltage spectra of nano-sized semiconductor and its applications in heterogeneous photocatalysis, Sol. Energy Mater. Sol. Cells 79 (2003) 133–151.
[20] L.Q. Jing, H.G. Fu, B.Q. Wang, D.J. Wang, B.F. Xin, S.D. Li, J.Z. Sun, Effects of Sn dopant on the photoinduced charge property and photocatalytic activity of TiO_2 nanoparticles, Appl. Catal. B 62 (2006) 282–291.
[21] H. Zhang, J.F. Banfield, Understanding polymorphic phase transformation behavior during growth of nanocrystalline aggregates: insights from TiO_2, J. Phys. Chem. B 104 (2000) 3481–3487.
[22] G.A. Tompsett, G.A. Bowmaker, R.P. Cooney, J.B. Metson, K.A. Rogers, J.M. Seakins, The Raman spectrum of brookite, TiO_2 (Pbca, $Z = 8$), J. Raman Spectrosc. 26 (1995) 57–62.
[23] X.Z. Ding, X.H. Liu, Correlation between anatase-to-rutile transformation and grain growth in nanocrystalline titania powders, J. Mater. Res. 13 (1998) 2556–2559.
[24] S. Brunauer, L. Deming, W.E. Deming, On a theory of the van der Waals adsorption of gases, J. Am. Chem. Soc. 62 (1940) 1723–1732.
[25] K.N.P. Kumar, J. Kumar, K. Keizer, Effect of peptization on densification and phase transformation behavior of sol–gel derived nanostructured titania, J. Am. Ceram. Soc. 77 (1994) 396–400.

[26] R. Asahi, T. Morikawa, T. Ohwaki, K. Aoki, Y. Taga, Visible-light photocatalysis in nitrogen-doped titanium oxides, Science 293 (2001) 269–271.
[27] T. Morikawa, R. Asahi, T. Ohwaki, K. Aoki, Y. Taga, Band-gap narrowing of titanium dioxide by nitrogen doping, Jpn. J. Appl. Phys. 40 (2001) 561–563.
[28] H. Irie, Y. Watanable, K. Hashimoto, Nitrogen-concentration dependence on photocatalytic activity of $TiO_{2-x}N_x$ powders, J. Phys. Chem. B 107 (2003) 5483–5486.
[29] W.J. Ren, Z.H. Ai, F.L. Jia, L.Z. Zhang, X.X. Fan, Z.G. Zou, Low temperature preparation and visible light photocatalytic activity of mesoporous carbon-doped crystalline TiO_2, Appl. Catal. B 69 (2007) 138–144.
[30] H. Tang, K. Prasad, R. Sanjines, P.E. Schmid, F. Levy, Electrical and optical properties of TiO_2 anatase thin films, J. Appl. Phys. 75 (1994) 2042–2047.
[31] L.Q. Jing, B.F. Xin, F.L. Yuan, B.Q. Wang, K.Y. Shi, W.M. Cai, H.G. Fu, Deactivation and regeneration of ZnO and TiO_2 nanoparticles in the gas phase photocatalytic oxidation of n-C_7H_{16} or SO_2, Appl. Catal. A 275 (2004) 49–54.
[32] J.C. Yu, L.Z. Zhang, J.G. Yu, Direct sonochemical preparation and characterization of highly active mesoporous TiO_2 with a bicrystalline framework, Chem. Mater. 14 (2002) 4647–4653.
[33] J.C. Yu, J. Lin, R.W.M. Kwok, Enhanced photocatalytic activity of $Ti_{1-x}V_xO_2$ solid solution on the degradation of acetone, J. Photochem. Photobiol. A: Chem. 111 (1997) 199–203.